Membrane Localization and Dynamics of Geranylgeranylated Rab5 Hypervariable Region

Eileen Edler[a], Eric Schulze[a,b], Matthias Stein[a*]

[a]Molecular Simulations and Design Group, Max Planck Institute for Dynamics of Complex Technical Systems, Sandtorstrasse 1, 39106 Magdeburg, Germany.

[b]International Max Planck Research School (IMPRS) for Advanced Methods in Process and Systems Engineering, Magdeburg, Germany.

*Corresponding author: Dr Matthias Stein, Molecular Simulations and Design Group, Max Planck Institute for Dynamics of Complex Technical Systems, Sandtorstrasse 1, 39106 Magdeburg, Germany. Email Matthias.stein@mpi-magdeburg.mpg.de, fax +49 391 6110 436.

Abstract

The small GTPase Rab5 is a key regulator of endosomal trafficking processes and a marker for the early endosome. The C-terminal hypervariable region (HVR) of Rab5 is post-translationally modified at residues Cys^{212} and Cys^{213} to accommodate two geranylgeranyl anchors (C20 carbon chain length) in order to associate Rab5 with the membrane. The structural role of the HVR regarding protein-early endosome membrane recruitment is not resolved due to its high degree of flexibility and lack of crystallographic information. Here, full-atomistic and coarse-grained molecular dynamics simulations of the truncated Rab5 $HVR^{206-215}$ in three model membranes of increasing complexity (pure phospholipid bilayer, ternary membrane with cholesterol, six-component early endosome) were performed. Specific electrostatic interactions between the $HVR^{206-215}$ Arg209 residue and the phosphate group of the inositol ring of PI(3)P were detected. This shows that PI(3)P acts as a first contact site of protein recruitment to the early endosome. The free energy change of $HVR^{206-215}$ extraction from the bilayer was largest for the physiological negatively charged membrane. 5 µs coarse-grained simulations revealed an active recruitment of PI(3)P to the $HVR^{206-215}$ supporting the formation of Rab5- and PI(3)P enriched signaling platforms.

Keywords

- Small GTPase
- Peripheral membrane protein
- Molecular dynamics
- Hypervariable region
- Lipid enrichment
- Lipid-protein interactions

1. Introduction

Rab GTPases are key regulators of vesicular transport between different intracellular compartments in eukaryotic cells. As peripheral membrane proteins they are post-translationally modified by fatty acid chains which anchor them to the membrane. This lipid anchor is covalently attached within a C-terminal hypervariable region (HVR) which has a disordered structure and is thus highly flexible. The role of the HVR is controversially discussed in literature [1, 2] and it remains still unclear if Rab targeting to specific cellular membranes is HVR-dependent. The HVR is the linker between the catalytic GTPase domain (G domain) and the membrane anchor; however, its concrete function varies between different members of the Rab family. In some cases, e.g. Rab7 and Rab35, the HVR is essential for specific Rab targeting [3]. Hydrophobic lipid anchors are distinguished according to their structure (branched or unbranched) and their chain length. Common lipid anchors are branched isoprenyl groups like geranylgeranyl or farnesyl chains, saturated fatty acids like palmitoyl chains, sterol groups or glycophosphatidylinositol (GPI) anchors. The partitioning of membrane proteins into raft regions, i.e. dynamic lateral substructures rich in sphingolipids and cholesterol [4, 5], or non-raft regions appears to depend on the type of lipid modification. Saturated lipid moieties, GPI as well as sterol anchors are known to target proteins into raft-like domains. On the other hand, short unsaturated or branched lipid modifications counteract a partitioning into highly ordered raft domains [6]. However, it is still under debate to what extent lipid anchors affect protein sorting and membrane organization and which other factors may be involved [7-9]. Observations suggest that apart from pure liquid ordered (Lo) – liquid disordered (Ld) phase separation also the plasma membrane composition with regard to lipid-protein and protein-protein interactions is important for the phase preference of lipid anchored signaling proteins.

In this study we focus on a truncated Rab5 HVR (hereafter, $HVR^{206-215}$) with two geranylgeranyl (GG) chains covalently attached to residues Cys^{212} and Cys^{213} (Figure 1). Except for membrane binding via its GG anchor little is known about C-terminal Rab5-membrane interactions. Besides mainly polar uncharged amino acids the peptide contains

one positively charged arginine residue. Rab5 is associated with the regulation of early endosomal trafficking, vesicle budding, early endosomes fusion, phagocytic transport and micropinocytosis [10]. Previous molecular dynamics (MD) studies of full-length Rab5 revealed two different orientations of the catalytic G domain, resulting in the formation of multiple protein-lipid contacts [11]. A similar behavior with at least two dominant G domain binding modes was observed for full-length H-Ras [12] and K-Ras [13] in atomistic MD simulations. These membrane-associated orientational dynamics appear to be a general concept for a wide range of lipidated small GTPases [14]. In order to investigate the interactions between protein and lipids in more detail, model systems representing the membrane-anchored C-terminus of small GTPases, often a short peptide sequence, were analyzed in several studies. Experimental solid-state NMR and Fourier transform infrared spectroscopy as well as MD simulations were used to investigate N-Ras peptide dynamics in a DMPC lipid bilayer [15-19]. Moreover, MD simulations were performed, elucidating different conformational states of the lipidated, positively charged K-Ras C-terminus [20] and point to the role of charged lipids in membrane systems on protein binding [21].

Our MD study investigates the Rab5 $HVR^{206-215}$ bound to membranes of different lipid composition in a multiscale approach. The highly flexible $HVR^{206-215}$ showed several distinct conformational states. Electrostatic interactions between the charged PI(3)P signaling lipid and the protein arginine amino acid residue were observed and indicate a membrane-protein recruitment site. The potential of mean force of the GG anchor extraction by steered MD and umbrella sampling method showed that these electrostatic interactions with the charged membrane persist after the GG anchor was completely removed from the bilayer. We employed long-term coarse-grained MD simulations to sufficiently sample the lipid diffusion in membranes which revealed a significant accumulation of cholesterol and PI(3)P in close proximity to the peptide.

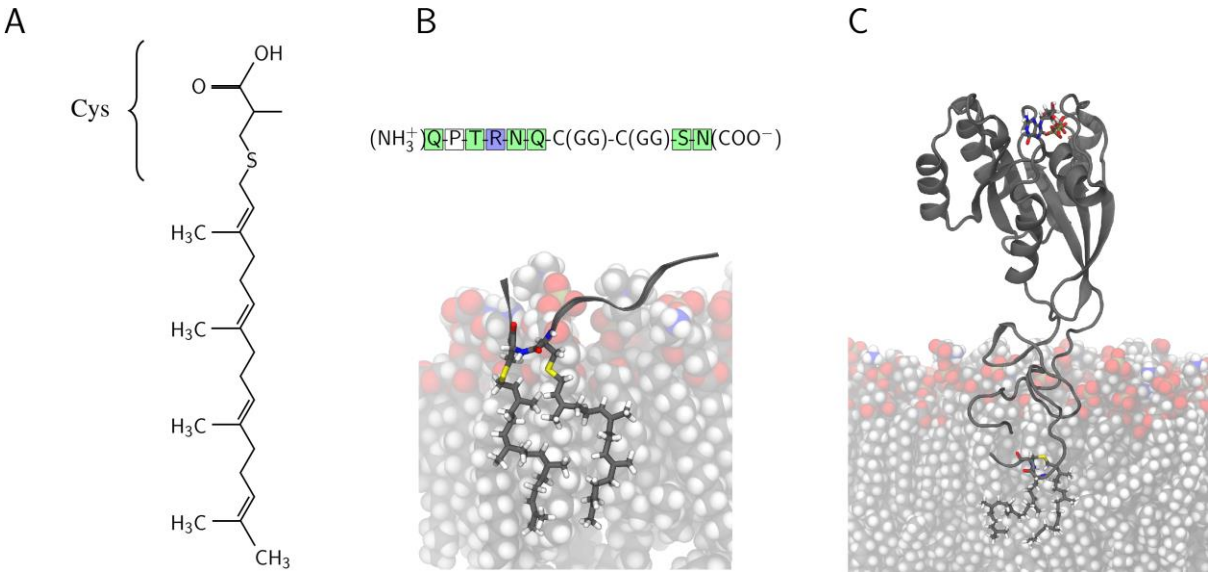

Figure 1 The geranylgeranyl (GG) chain is covalently attached to a protein cysteine residue **(A)**. Rab5 C-terminal $HVR^{206-215}$ sequence (top) and structure of two GG chains in the membrane **(B).** MD simulated full-sequence Rab5 protein binding to the membrane **(C)**.

2. Methods

2.1 Protein structure preparation and parameterization of the lipid anchor

We constructed a $HVR^{206-215}$ model of the C-terminal residues of the Rab5 protein: (NH_3^+)Gln-Pro-Thr-Arg-Asn-Gln-Cys(GG)-Cys(GG)-Ser-Asn(COO^-), with GG presenting the geranylgeranyl chains covalently bound to the cysteine residues Cys212 and Cys213. In all-atom simulations the lipid modifications were modeled using parameters derived from the CHARMM36 force field [22, 23]. Structural properties of the anchors (bond lengths, bond angles, dihedrals) were validated against optimized structures from quantum-mechanical DFT calculations with TURBOMOLE V6.6 [24]. Geometry optimizations were performed with a split-valence basis set (def2-SVP) [25] using the pure BP86 functional [26, 27] and the conductor-like screening model (COSMO) [28] with a dielectric constant of ε=2 in order to mimic the hydrophobic core region of the surrounding membrane lipids [29].

The protein C-terminus starting structure was obtained from a full-sequence Rab5 structure minimized for 20,000 steps by conjugate gradient and refined in 250 ns MD simulations with CHARMM36 force field [11].

2.2 Membrane Models

Three symmetric model membranes of different lipid compositions were built. For pure palmitoyl-oleoyl-phosphatidylcholine (POPC) the VMD Membrane Plugin [30] was used. The ternary and six-component membranes were built with the CHARMM-GUI Membrane Builder [31, 32]. The POPC membrane represents a neutral, zwitterionic model bilayer. The ternary

membrane is a combination of lipids often used as a simple model for the plasma membrane featuring cholesterol and sphingolipids which are crucial for ordered raft domains [33]. The composition of the six-component membrane was chosen according to the inner leaflet of the mammalian plasma membrane [34]. The level of phosphatidylinositol 3-phosphate (PI(3)P) is adjusted to that of the early endosome membrane. The lipid compositions and the dimensions of membrane planes are given in Table 1.

Table 1
Composition and lateral dimensions of the three model membrane systems. Abbreviations as follows; POPC: palmitoyl-oleoyl-phosphatidylcholine, CHOL: cholesterol, PSM: palmitoyl-sphingomyelin, POPE: palmitoyl-oleoyl-phosphatidylethanolamine, POPS: palmitoyl-oleoyl-phosphatidylserine, PI(3)P: phosphatidylinositol 3-phosphate.

Membrane system	Component	Number of lipids (ratio)	Lateral (x,y) dimensions / nm
Pure POPC	POPC	2 x 273 (100%)	15.7 x 14.9
Ternary	POPC	2 x 166 (40%)	14.8 x 14.4
	CHOL	2 x 166 (40%)	
	PSM	2 x 83 (20%)	
Six-component	POPC	2 x 90 (17.8%)	16.9 x 16.6
	CHOL	2 x 150 (29.7%)	
	PSM	2 x 50 (9.9%)	
	POPE	2 x 135 (26.7%)	
	POPS	2 x 55 (10.9%)	
	PI(3)P	2 x 25 (5.0%)	

2.3 All-Atom Simulation Protocol

Prior to the $HVR^{206-215}$-bilayer study, each membrane system without peptides was energy minimized with a conjugate gradient algorithm, heated to a temperature of 310 K and equilibrated in a 50 ns MD simulation using NAMD 2.9 [35]. The CHARMM36 force fields for proteins and lipids were used for the full-atomistic MD simulations [22, 23, 36, 37]. Insertion of lipids was realized by randomly replacing one POPC lipid by the two GG anchors of the $HVR^{206-215}$. For sufficient sampling six $HVR^{206-215}$ constructs were inserted into each membrane system. Except for the pure POPC bilayer, it was ensured that the lipid composition around each peptide was different within one membrane (see Supplementary Table S6). The systems were solvated with TIP3P water [38], neutralized, and ionized to a physiological salt concentration of 0.15 mol/L NaCl. Subsequently, energy minimization, heating to 310 K and 50 ns MD simulations of equilibration were performed. A 200 ns production simulation was performed for each membrane in an NPT ensemble. Constant temperature control of 310 K was achieved by Langevin dynamics. Periodic boundary conditions were applied at a standard pressure of 1.01 bar controlled by the Nosé-Hoover Langevin piston method as implemented in NAMD [39, 40]. Anisotropic cell fluctuations in all three spatial dimensions were possible at a constant x-y plane cell ratio. Electrostatic interactions were treated by the Particle Mesh Ewald (PME) method [41] in NAMD [42],

truncating van der Waals interactions at 12 Å and applying a switching function at 10 Å. The SHAKE algorithm was applied to all covalent bonds involving hydrogen atoms to allow for a 2 fs time step.

2.4 Steered MD and umbrella sampling

After 250 ns all-atom MD production runs with six $HVR^{206-215}$ replicates, all three peptide-membrane systems were subjected to constant-velocity steered MD (SMD) simulations in order to generate initial structures for umbrella sampling windows. The simulation box was adjusted to the size of one $HVR^{206-215}$ in x, y-dimensions and elongated along the bilayer normal in z-dimension. From each model membrane three arbitrarily chosen peptides with two GG chains were independently pulled out of the membrane with a constant velocity of 5 Å/ns and a force constant of 2.4 kcal/mol/$Å^2$. The force constant was chosen large enough to ensure that the reaction coordinate follows the constraint position but not so high it restrains thermal motions too excessively [43-46]. The potential was applied to the Cα atoms of both CysGG residues. Pulling was monitored over a period of 8 ns. Umbrella sampling was performed for 25 ns in each of up to 31 independent windows covering a total z-distance of about 4 nm in steps of 0.13 nm. Thus, the umbrella sampling simulations yielded a total of 2 µs for the GG anchor bilayer-to-water transfer in pure POPC and the ternary mixture, i.e. 25 ns at each of 27 windows repeated for three $HVR^{206-215}$ replicates. For the six-component membrane the duration of the umbrella sampling was 2.3 µs in total, i.e. 25 ns at each of 31 windows for three $HVR^{206-215}$ replicates. During umbrella sampling the lipid P atoms were restrained in z direction. The actual force constant for the collective variable was 4 kcal/mol/$Å^2$. The potential of mean force (PMF) was calculated from the average of three independent umbrella sampling calculations in one membrane system using the weighted histogram analysis method (WHAM) [47] implemented by Alan Grossfield [48].

2.5 Coarse-grained MD simulation with MARTINI

For long time scale MD studies, the three phospholipid bilayer systems were also modeled using coarse-grained MD simulations. In addition, a charged five-component model membrane was investigated lacking the signaling lipid PI(3)P. Membrane formation and insertion of the GG anchor chains was performed using a modified version of the Python tool *insane.py* [49] (available upon request). The $HVR^{206-215}$ was inserted into the membrane by adjusting the length of the GG chains to match the length of the fatty acid chains of the bilayer. A maximum solvent exposure of the peptide backbone was ensured. The tool places the $HVR^{206-215}$ in the geometric center of the bilayer and automatically detects and removes

overlapping lipids. In the mixed bilayers the lipids are distributed randomly. The pseudo-random numbers are generated by the Python module *random* which uses the Mersenne Twister algorithm. The systems were solvated with MARTINI water (9:1 mixture of solvent and anti-freeze particles) and ions were added to model an ionic strength of 0.15 mol/L NaCl.

All topologies utilized standard MARTINI 2.2 particle definitions. For POPC, POPE, POPS and CHOL, the MARTINI lipid topologies ver. 2 were used [49]. For PSM the topology of DPSM ver. 1 was used. PI(3)P was modeled from the topologies of PAPI ver. 1 for the backbone and tails, and POP1 ver. 1 for the phosphorylated inositol head group (see PI(3)P topology in SI). The $HVR^{206-215}$ was modeled by coarse-graining a structure of the previously derived all-atom model of the full-length Rab5 protein according to standard MARTINI [50] and MARTINI protein [51] rules implemented in the *martinize.py* tool (ver. 2.4). A detailed description of the GG anchor mapping is given in the results section.

All CG simulations were carried out using GROMACS [52] Ver. 5.0.7 and current MARTINI simulation input parameters [53]. Briefly, a Verlet cutoff scheme was used, with a buffer tolerance of 0.005 and neighbor list updating of every 20 steps. Electrostatic interactions were treated with a reaction-field, a Coulomb cutoff of 1.1 nm, and dielectric constant of 15. Van-der-Waals interactions had a cutoff of 1.1 nm and used a potential shift Verlet modifier. HVR, solvent and membrane were coupled to individual velocity-rescaling thermostats with a coupling constant of 1 and a reference temperature of 310 K. The systems were minimized for 1000 steps using steepest descent, and equilibrated for 0.5 ns in an NVT ensemble using a step size of 10 fs, and relaxed for 30 ns with a 20 fs time step in an NPT ensemble controlled by a semi-isotropic Berendsen barostat [54]. The compressibility was set to $3 \cdot 10^{-4}$ with a coupling-constant of 12 and a reference pressure of 1 atm. 5 µs production runs were performed with a time step of 20 fs and the Parinello-Rahman barostat [55].

2.5 Analysis of HVR structural parameters and diffusion

The dihedral angle distribution of the all-atom GG force field parameters and the coarse-grain mapping of the GG anchor were validated against quantum chemical DFT calculations of torsional energy profiles. Different structural lipid parameters (e.g. bilayer thickness, area per lipid, lipid order parameters, lipid head group orientation, and acyl chain orientation) were calculated to allow a comparison between the three membranes and with experiment. Coordinates were selected and extracted from the MD trajectories via MDAnalysis [56]. In a similar fashion to the GridMAT-MD program [57], Voronoi tessellation was used to map lipid molecules to their (periodically) nearest points on a grid (200 x 200 cells). The phospholipid head groups served as reference points. Like in GridMAT-MD, the tessellation was used to

estimate the local thickness of the lipid bilayer by determining the difference in z-coordinates of each lipid and its closest neighbor on the opposite leaflet of the bilayer. The difference was mapped onto the grid points of that particular lipid. In addition, the acyl chain order parameters were determined, averaged over all carbon atoms of one chain and mapped onto the grid. Relative local properties were averaged over the entire 200 ns of simulation and shown as the difference from the global average value. Calculation of membrane properties at varying cutoff distances around the GG anchors were performed accordingly. The calculation of acyl chain order parameters was performed using the approach of Douliez et al. [58] for the saturated palmitoyl chains of POPC, PSM, POPE and POPS at the glycerol *sn-1* position. For PC, PE, PS, and PSM the head group orientation is defined as the angle between the bilayer normal, n, and the direction vector between the phosphorous and nitrogen atoms (PN vector) (Figure 2A). For cholesterol, instead of the PN vector, the vector between C3 and C17 was used (Figure 2B). In the case of PI(3)P, the inositol tilt angle was computed, which is defined as the angle between membrane normal and the vector from C1 to C4 of the inositol ring (Figure 2C). Phospholipid tail orientations were determined by the angle between the vector connecting the central glycerol backbone carbon with the last fatty acid carbon atoms of both chains and the membrane normal (Figure 2D).

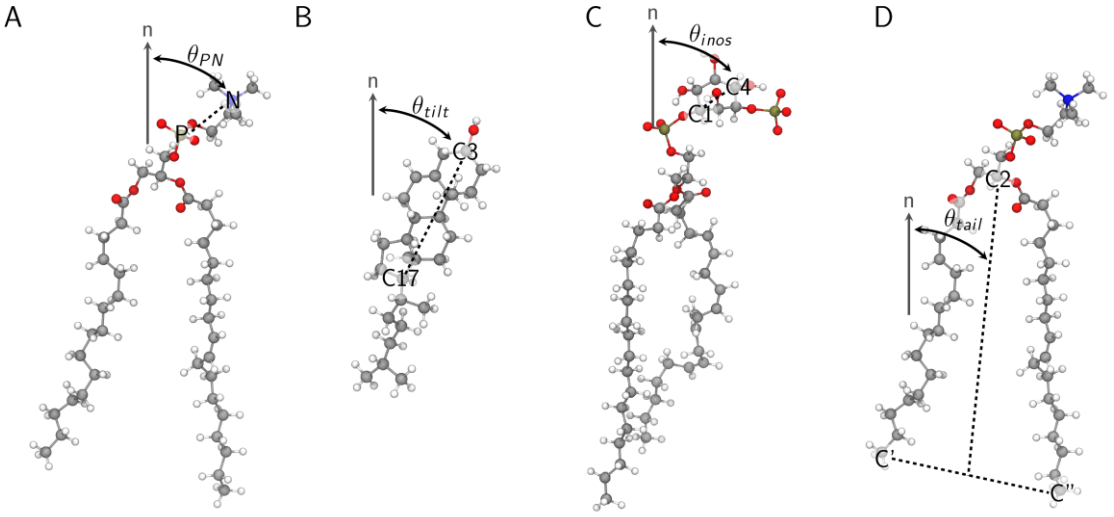

Figure 2 Orientation of lipids relative to the membrane. θ was defined as the angle between the membrane normal and the corresponding direction vectors describing **A)** the head group orientation of POPC, POPE, POPS, PSM, **B)** the tilt angle of cholesterol, **C)** the inositol ring orientation of PI(3)P, and **D)** the phospholipid tail orientation of POPC, POPE, POPS, PSM, and PI(3)P.

Peptide-specific observables (anchor insertion depth, root mean square fluctuation (RMSF), radius of gyration, solvent-accessible surface area (SASA)) and diffusion coefficients were calculated to investigate the membrane composition-dependent behavior of the Rab5 $HVR^{206-215}$. The anchor insertion depth is the z-distance between neighboring phospholipid P atoms and the lowest GG carbon atom (Fig. S9A). Similarly, the peptide-to-bilayer distance

is defined as the z-distance between the amino acid Cα atom and the surrounding phospholipid P atoms. Negative values, therefore, correspond to amino acids that are incorporated in the hydrophobic bilayer. The solvent exposure of the peptide amino acids was calculated as the relative SASA in VMD with a solvent probe radius of 1.4 Å according to Miller *et al.* [59]. For the SASA of the CysGG, a tripeptide of Gly-CysGG-Gly with a fully extended GG chain was energy minimized for 30,000 steps in explicit water and gave a maximum SASA of 724 $Å^2$. Lipid P atoms within a cutoff of 0.5 nm around the $HVR^{206-215}$ were counted to be lipid neighbors. In addition, dihedral angle principal component analysis (dPCA) was performed to reveal the free energy landscape of the $HVR^{206-215}$ in different bilayers [60-62]. Accordingly, the 18 dihedral angles (i.e. Ψ_1, Φ_2, Ψ_2,…, Φ_{10}) of the peptide were sine- and cosine-transformed, and the resulting covariance matrix was diagonalized to obtain the principal components. The peptide free energy landscapes were constructed using the first two principal components [60]. The influence of different dihedral angles on the first two principal components the loadings were calculated according to Altis *et al.* [61]. For the calculation of lateral diffusion coefficients the jump distance analysis (JDA) method [63] was used instead of mean square displacement (MSD), since it enabled us to compute the diffusion coefficient of single molecules with a satisfying accuracy. It showed a reduced standard deviation for small ensembles of fewer than 100 molecules and gave reasonable results in single particle tracking experiments [64].

3. Results and Discussion

3.1 Parameters of the geranylgeranyl membrane anchor

3.1.1. All-atom MD simulations

Since parameters for unsaturated branched hydrocarbon chains like the farnesyl (C15) and geranylgeranyl (C20) attached to a cysteine residue were not available in the CHARMM36 force field at the beginning of our study, we assigned the missing force field parameters. For full-atomistic MD simulations the topologies and parameters given in the CHARMM36 force fields for lipids [23] and proteins [22] were carefully assigned, re-validated against QM calculations and combined to give the reliable structural parameters for the GG chains (Supplementary Figure S1, Supplementary Table S1). The quality of the modeled anchor structures was compared with structurally optimized DFT models. Structural parameters (i.e. bond lengths, bond angles, torsion angles) agreed well with the results from DFT within less than 0.004 nm and 3.5° (Supplementary Table S2, Table S3, Table S4). Four critical dihedral angles were identified in the MD simulations, which corresponded to energy minima of the quantum chemically calculated torsional profiles (Figure 3). This supports the reliability

of the force field parameters to accurately describe the structural preferences and dynamic behavior of the GG chains in the phospholipid bilayer.

These identified torsion types reflect the repeating units of the GG chains. Torsion around a C-C single bond with one terminal C=C bond gave broad distributions enclosing a frequently visited average of ±100° with an energy barrier of 28 kJ/mol at 0° (Figure 3A, Supplementary Figure S2). As expected, rotation around a C=C bond resulted in very high energy barriers (≥150 kJ/mol) at ±90° yielding observed dihedrals exclusively at 0° (*cis* conformation) or ±180° (*trans* conformation), respectively (Figure 3B). A chain of single bonded C atoms including one central sp^2 hybridized carbon mainly adopted dihedral angles at ±90° with energy barriers of approximately 15 kJ/mol and 25 kJ/mol at 0° and ±135°, respectively (Figure 3C). A slightly shifted torsional profile was calculated for a chain of single bonded carbon atoms with two terminal sp^2 hybridized C atoms. Here, most of torsion angles were found at ±180° and small fractions around ±80° with an energy barrier of 25 kJ/mol at 0° (Figure 3D).

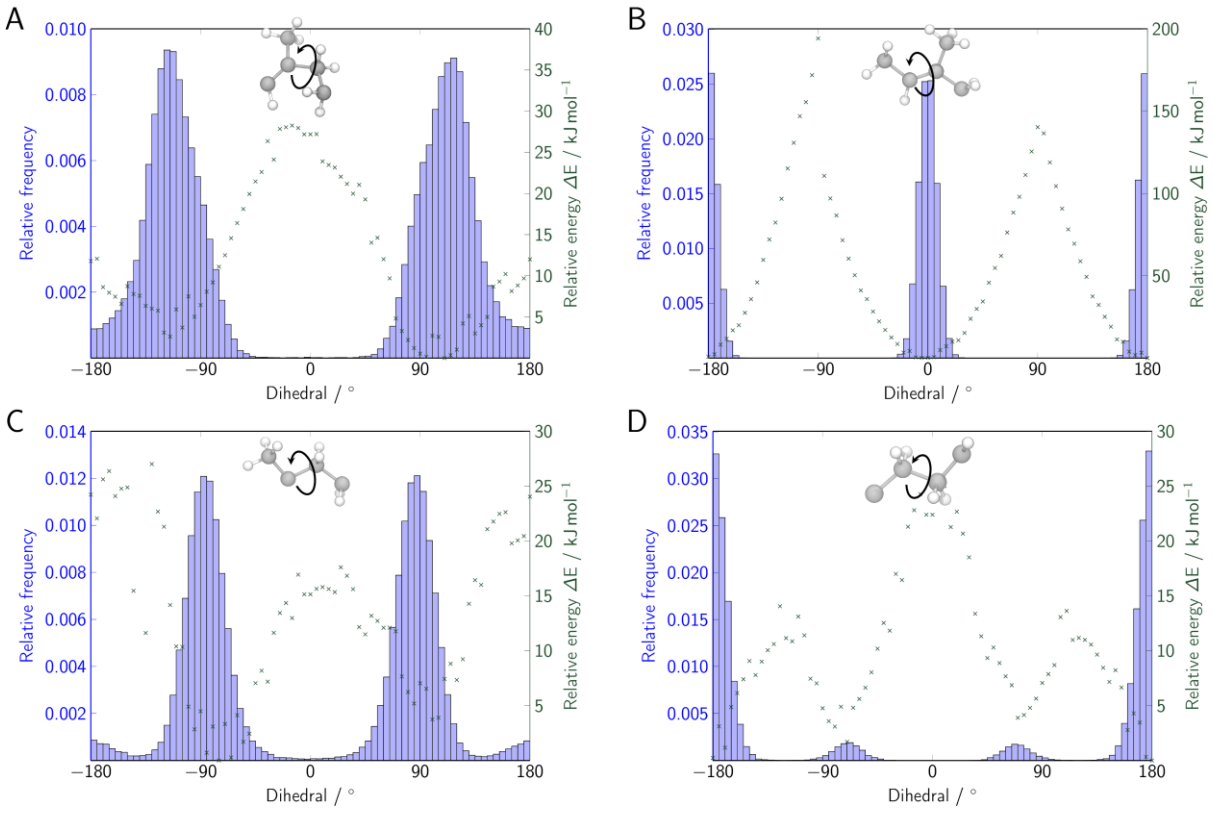

Figure 3 Comparison of MD-sampled dihedral angles of the GG anchor (left axis, blue bar plot ■) and the torsional energy profile from QM calculations (right axis, green crosses). Torsion around **A)** ϕ(CEL1-CEL1-CTL2-CTL2), **B)** ϕ(X-CEL1-CEL1-X), **C)** ϕ(CTL3-CEL1-CTL2-CTL2), and **D)** ϕ(X-CTL2-CTL2-X). For nomenclature see SI.

Based on the all-atom parameterization of the GG chains, corresponding MARTINI bead types were defined to describe the lipid anchor in a coarse-grained environment (Figure 4, for details see supplementary material).

3.1.2 Martini coarse-grained parametrization and MD simulation

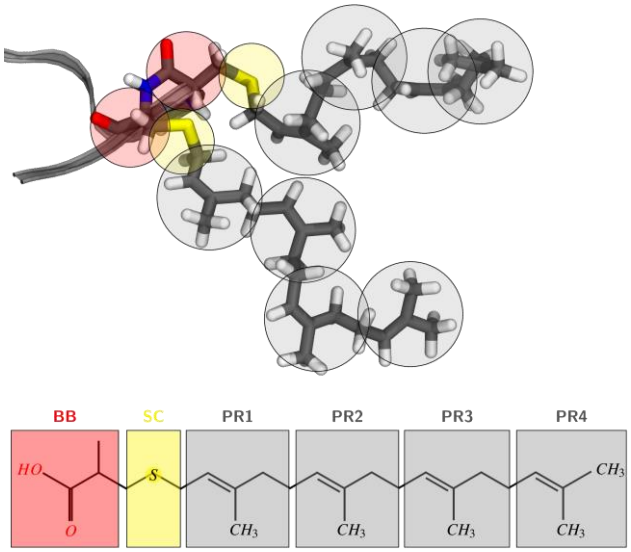

Figure 4 MARTINI bead types mapped on the CysGG residue.

The absence of topology and parameters for the GG chain in the MARTINI force field required a new definition for use in our coarse-grained simulations. The mapping of the amino acid backbone and the thiol group was adopted from the MARTINI protein force field [65]. The four prenyl groups of the GG chain were individually mapped to C3 beads, labeled PR1 to PR4. As typical for MARTINI, bond lengths use harmonic potentials and angles cosine-based potentials. In the input structure, the protein was inserted into a lipid bilayer in a fully extended GG chain conformation. For determination of secondary structure elements DSSP [66] was used treating post-translationally modified CysGG as a standard cysteine residue.

The CG bonded interactions were parameterized against a 200 ns all-atom simulation of the full-length protein in a pure POPC bilayer. In contrast to bond lengths and angles (Table 2), the dihedrals were not explicitly parameterized for the sake of stability and to prevent over-parameterization. Bond lengths, bond angles and dihedrals were found to reproduce the results of the all-atom simulations very well, the latter being sufficiently well estimated due to intramolecular non-bonded interactions (Supplementary Figure S3).

Table 2 Bond lengths in nm with harmonic force constants, bond angles in °, and cosine-based potential parameters for the coarse-grained CysGG residue.

Bond	Length / nm	Force constant / kJ/(mol nm^2)	Angle	Angle / °	Force constant / kJ/(mol rad^2)
BB-SC	0.31	20000	BB-SC-PR1	135	20
SC-PR1	0.37	10000	SC-PR1-PR2	115	25
PR1-PR2	0.46	7500	PR1-PR2-PR3	105	20
PR2-PR3	0.46	7500	PR2-PR3-PR4	100	20

PR3-PR4	0.46	7500

The MARTINI particle type specifies its non-bonded interactions. In order to justify the choice of C3 beads for the prenyl groups of the GG chain, an umbrella sampling of a bilayer-to-solvent transition was carried out, which was analyzed via the GROMACS tool *g_wham* (weighted histogram analysis method) [67]. The umbrella sampling was done with an Arg-Gly-CysGG peptide in a bilayer consisting of 90% POPC and 10% POPE. This setup was chosen to match experimental conditions used by Silvius et al. [68], who determined the affinities of GG peptides for a PC/PE bilayer in a fluorescence-enhancement assay. We computed a bilayer-to-water transition free energy difference ΔΔG of 32 kJ/mol (Supplementary Figure S4), which is slightly lower than the experimental value of 49 kJ/mol for the C-terminally methylated GG peptide. The uncharged fluorophoric dye used in experiments was approximated by modeling the N-terminal backbone bead as non-charged, hydrogen bond donating (Nd) bead. Experimentally, however, it was show that the influence of the dye is negligible on the free energy change.

3.2. Local peptide-induced changes to membrane properties

Insertion of a peptide into a bilayer may introduce changes in membrane structure and ordering. All-atom 200 ns simulations of each membrane system with six inserted $HVR^{206-215}$ replicates were performed to investigate lipid composition-dependent structural properties.

3.2.1 Membrane thickness and order parameters

First, in order to validate our simulations against experiment and previous MD simulations, we investigated membrane-specific properties. Thickness and lipid area of the pure POPC bilayer were in very good agreement with experimental values [69] (Supplementary Figure S5, Supplementary Table S5). We observed the well-described ordering effect of cholesterol in our mixed model membranes. Cholesterol increased the overall membrane thickness by inserting between the phospholipid hydrophobic chains in their extended configuration, leading to a denser packing and thus a decrease of area per lipid [70-72].

The acyl chain order parameters for the pure POPC membrane were in very good agreement with data derived by NMR experiments with POPC-cholesterol multi-lamellar vesicles (MLVs) [73]. With increasing amounts of cholesterol, the lipid order significantly increased (Supplementary Figure S6). The increase in order was 85.7% in the ternary mixture and 73.5% in the six-component membrane. The ordering of the acyl chains seemed to be independent of the head group since POPC, POPE and POPS showed almost identical profiles (Supplementary Figure S7). For PSM carbon atoms C7-C10, the order was higher compared to POPC, POPE or POPS suggesting that cholesterol increases the order

of PSM chains in direct neighborhood more prominently [74]. Lipid orientation angles, except for cholesterol, showed very broad distributions (Supplementary Figure S8, A-C). A smaller POPC orientation angle in the charged membrane may be associated with an re-arrangement of the P-N dipole in order to maximize electrostatic interactions with the negatively charged head groups of PI(3)P and PS located slightly above the lipid phosphate groups. Generally, head group size seemed to be more relevant to the orientation than the charge. The smaller ethanolamine head group of POPE exhibited a larger head group orientation angle with respect to the bilayer normal compared to PI(3)P, POPS, POPC, and PSM. This shows that the head group of PE was pointing toward the membrane interior as a consequence of less steric hindrance and strengthening electrostatic interactions with the negatively charged lipid phosphate groups. The inositol ring tilt angle of PI(3)P was in good agreement with values obtained in previous MD studies of PI(3)P in pure POPC or POPS bilayers [75]. Compared to the perpendicular orientation of cholesterol in the uncharged membranes, its orientation was tilted in the charged bilayer. The reorientation is related to the reduced order and thickness as well as the increased area per lipid compared to the ternary mixture. Also the acyl chain orientation of the phospholipids was determined (Supplementary Figure S8, D). Smaller acyl chain orientation angles reflect an extended orientation of the acyl chains and are a consequence of the higher order in cholesterol-containing membranes. PI(3)P in the charged membrane showed the largest angle due to the high degree of unsaturation in the acyl chain.

3.2.2 Lipid diffusion

Lateral diffusion of lipids can be easily measured experimentally and represents a suitable property to compare dynamical aspects of our simulations to experiment (Table 3). Since the number of lipids was small (e.g. 25 PI(3)P lipids in one layer) JDA method was superior to MSD measurements (see Methods). To validate the JDA procedure, the diffusion coefficient of 500 individual water molecules from each membrane simulation system was calculated. The average over all systems was around $440 \cdot 10^{-7}$ cm^2s^{-1}, which is comparable to TIP3P water diffusion derived from MD studies ($520 \cdot 10^{-7}$ cm^2s^{-1} at 300 K) [76] and only slightly larger than experimental findings ($322 \cdot 10^{-7}$ cm^2s^{-1} at 313 K) [77]. In pure POPC, diffusion was $1.36 \cdot 10^{-7}$ cm^2s^{-1} and in very good agreement with experimental data from NMR studies [78]. Inclusion of cholesterol reduced the diffusion of POPC by up to 45.6%. In the six-component charged membrane diffusion was very similar for all lipid types (between $0.59 \cdot 10^{-7}$ cm^2s^{-1} to $0.68 \cdot 10^{-7}$ cm^2s^{-1}). Apparently lipid diffusion in the membrane systems was slow, and a thorough mixing was not achievable in 200 ns of all-atom MD simulations. Diffusional studies elucidating changes in the lipid composition close to the inserted peptides were therefore performed on larger timescales using CG simulations.

Table 3 Lateral diffusion coefficients from 200 ns all-atom MD simulations in the three investigated membrane systems calculated by JDA.

Diffusion coefficient / 10^{-7} cm^2s^{-1}	Pure POPC	Ternary	Six-component
Water	429.67 ± 136.05	451.28 ± 61.85	445.94 ± 63.65
Lipids			
POPC	1.36 ± 0. 46	0.78 ± 0.23	0.74 ± 0.19
PSM		0.60 ± 0.18	0.62 ± 0.16
CHOL		0.59 ± 0.13	0.59 ± 0.11
POPE			0.68 ± 0.18
POPS			0.65 ± 0.17
PI(3)P			0.62 ± 0.16

3.2.3 Local membrane structure perturbations

Integral membrane proteins are known to significantly alter the structure of their surrounding lipid environment. To assess the effect of the peripheral $HVR^{206-215}$ on the bilayer, local membrane properties in a radius of up to 5 nm around the HVR were investigated. Therefore, we employed Voronoi tessellation with a fine resolution grid mapping and calculated the local bilayer thickness and acyl chain order parameters for the individual Voronoi cells (Figure 5). The three membrane systems are shown in top view with the $HVR^{206-215}$ marked as black crosses. Local deviations, i.e. ±4% for thickness and approximately ±20% for order parameters, were observed for all model membranes and are independent of different lipid compositions. As expected, regions of increased membrane thickness were higher ordered. In close proximity to the GG anchors, a small reduction of membrane thickness was accompanied by a moderate reduction in order.

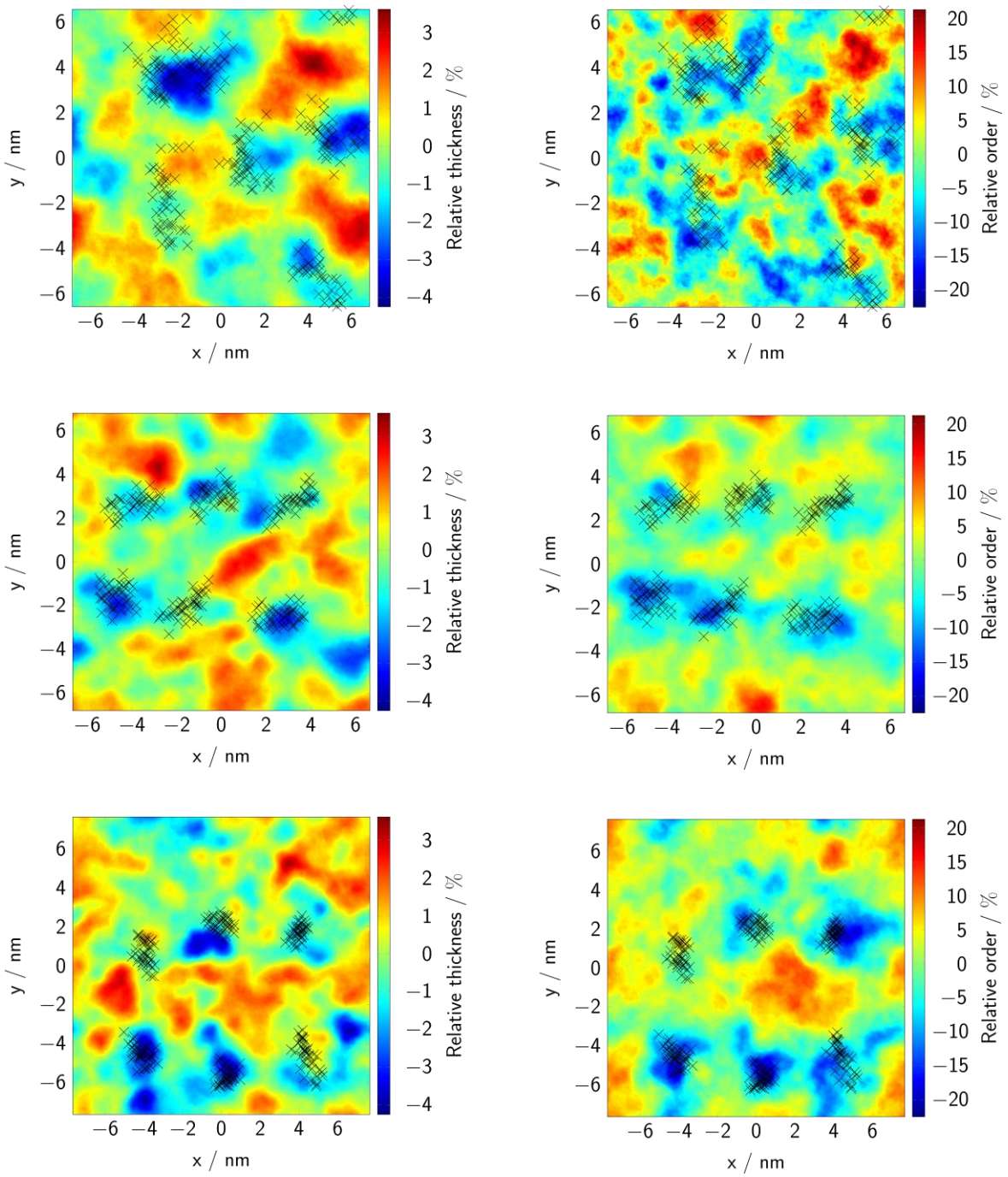

Figure 5 Local variations in membrane thickness (left) and lipid order (right) are shown for the membrane systems of pure POPC (top), the ternary mixture (center) and the six-component membrane (bottom). The positions of the GG anchors are marked with black crosses.

Membrane properties (thickness, acyl chain order, lipid head group orientation, and acyl chain orientation) as a function of distance to the anchor are shown in Figure 6. Here, it was confirmed that the local thickness decrease close to the GG chains was only small, however, it was largest in the negatively charged six-component membrane (Figure 6A). This is in agreement with MD simulations of a Ras peptide in pure DMPC [16]. The acyl chain order was reduced around the inserted peptides (Figure 6B). This is a consequence of the order

reduction in the GG anchor due to the adaptation of the peptide anchor to the surrounding lipid chain length [15, 16, 18]. The acyl chain order was most reduced in the pure POPC membrane where the lipid chains are not stabilized by cholesterol. Accordingly, the POPC lipid head group orientation angle in close proximity to the peptides was reduced by more than 6% in pure POPC (Figure 6C), i.e. the head groups were less tilted compared to average. In contrast, the cholesterol-stabilized POPC lipids in the ternary mixture as well as in the six-component membrane were less affected by the peptide. The chain orientation angle, a measure for the lipid tail orientation, was increased in all membrane systems but most significantly in the charged membrane by over 16% (Figure 6D). An increased chain orientation angle is associated with a tilted orientation of the acyl chain and directly related to the decreased lipid order.

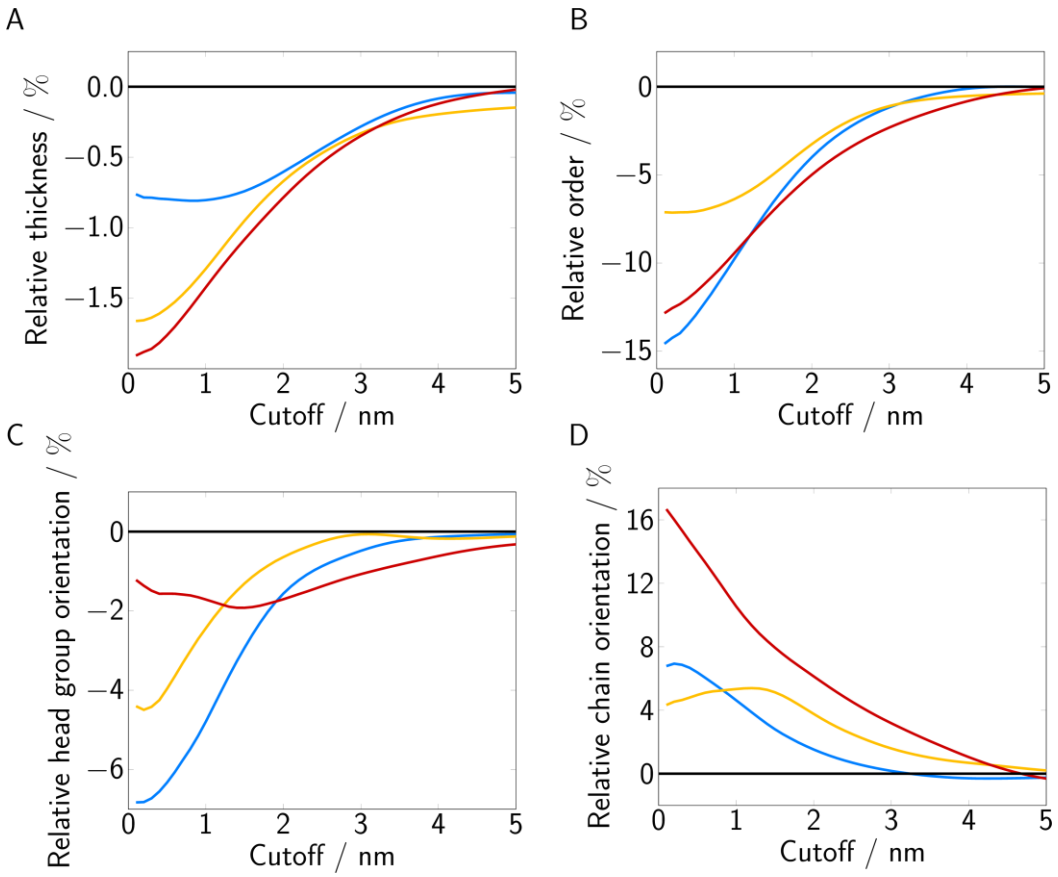

Figure 6 A) Membrane thickness, **B)** acyl chain order parameter, **C)** lipid head group orientation, and **D)** acyl chain orientation are presented as functions of the cutoff around the $HVR^{206-215}$. Data represent the percentage difference from global average. Data are shown for pure POPC (blue), the ternary membrane (yellow) and the six-component membrane (red).

3.3. HVR$^{206-215}$ structure and dynamics in the membrane

3.3.1 Structure of membrane-anchored HVR

When investigating the dynamical behavior of the geranylgeranyl anchors in the different membrane systems, we observed that the two adjacent GG chains in one HVR$^{206-215}$ moiety showed anti-correlated motions (Supplementary Figure S9, A-B). That is, if one chain was deeply inserted within the bilayer, the other chain was allowed to bend towards the membrane surface. This energetically favorable behavior ensures a high degree of dynamic flexibility, similar to that shown for a truncated C-terminal Ras heptapeptide modified with two hexadecyl chains [19]. The average insertion depth was depending on the absolute thickness of the surrounding bilayer and was always 38-39% of the bilayer thickness (Supplementary Figure S9, C). This observation indicates that the geranylgeranyl anchor does not penetrate the highly unordered region close to center of the bilayer. This is in agreement with ^{2}H solid-state NMR experiments providing evidence that the anchors adapt their insertion depths to the surrounding lipids [79, 80]. The reduction of hydrophobic mismatch between the anchor chains and the lipid tails is mainly driven by the regulation of the anchor insertion depth rather than by adapting the z extension of the surrounding lipid tails.

In our MD simulations the Rab5 HVR$^{206-215}$ was remarkably flexible. It employed a fully disordered structure without forming any secondary structure elements stabilized by intramolecular hydrogen bonds. According to the Ramachandran plot [81] represented in Supplementary Figure S10A, the most frequently populated region corresponded to the extended beta sheet conformations for $-160° \leq \Phi \leq -45°$ and $90° \leq \Psi \leq 180°$. With increasing distance from the anchoring residues, which tie the peptide to the membrane, the root mean square fluctuations (RMSF) increased significantly (Supplementary Figure S10, B). However, the peptide RMSF was independent of the membrane composition. Another measure for the HVR$^{206-215}$ flexibility is the radius of gyration (Supplementary Figure S10, C), which was only marginally greater in the negatively charged membrane compared to the uncharged bilayers. The exact lipid compositions around the individual HVR replicates as well as local structural and dynamic properties are given in Supplementary Table S6.

Snapshots from the HVR$^{206-215}$ in the charged membrane show that the majority of protein residues resided close to the membrane surface in the lipid water interface (Supplementary Figure S10, D). Especially the basic Arg209 was involved in electrostatic interactions with the negatively charged bilayer, by forming contacts with the protruding phosphate groups of the inositol ring of PI(3)P. In contrast, in the uncharged membranes Arg209 protruded more into the phospholipid head group zone by establishing strong electrostatic interactions with the negatively charged phosphate groups. Residues at large distance from the anchoring

GG chains (i.e. at the N-terminus) were pointing from the bilayer surface and were water exposed in order to maximize solubility (Supplementary Figure S11).

Recent studies showed that charged lipids facilitate binding of peripheral membrane proteins via the pleckstrin homology (PH) [82, 83], the PTEN-like domain [84] or single basic amino acids [85] by attracting certain residues towards the membrane surface. The interaction between the $HVR^{206-215}$ Arg209 and the signaling lipid PI(3)P may represent a first step in phospholipid signaling and protein recruitment to the early endosome.

Both the solvent-accessible surface area (SASA) and the number of neighboring lipid atoms (Figure 7) per HVR amino acid residue do not vary significantly between different membrane composition but display large differences between the individual HVR replicates. This again indicates the large structural flexibility of the $HVR^{206-215}$, even when anchored to the membrane and protein-membrane interactions come into play.

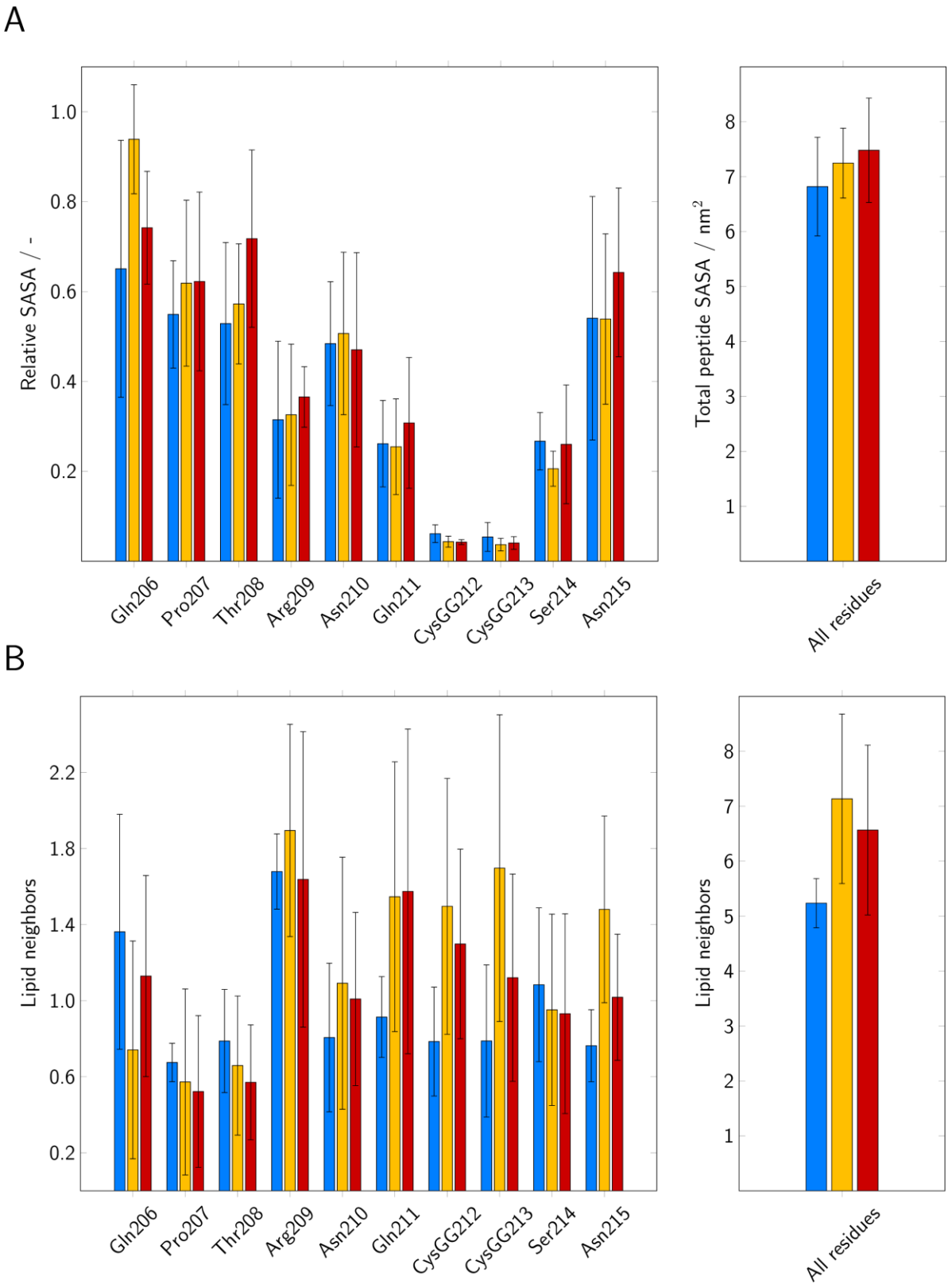

Figure 7 HVR$^{206\text{-}215}$-membrane interactions were characterized in terms of **A)** solvent-accessible surface area and **B)** the number of lipid neighbors (within a radius of 0.5 nm). Data were averaged over 200 ns of MD simulations and the six HVR$^{206\text{-}215}$ replicates in pure POPC (blue), the ternary mixture (yellow), and the six-component membrane (red). Error bars represent the standard deviation between the six replicates.

In order to investigate whether certain combinations of dihedrals in the HVR$^{206-215}$ were associated with a specific membrane composition we performed a dihedral angle principal component analysis (dPCA). This method is a valuable tool for constructing the free energy landscape of flexible peptides due to the separation of internal and overall motion (see Methods) [60-62]. The free energy surfaces of the six truncated HVR domains in the three membrane systems were obtained along the first two eigenvectors, V1 and V2, which explained 45% to 50% of the protein structural variance (Figure 8 and Supplementary Figure S12, Supplementary Figure S13). Dihedral PCA-based clustering revealed 4-5 distinct conformational states, which were membrane composition- and charge-independent.

We also investigated which dihedral angles were responsible for the first two principal components (Supplementary Figure S14). For peptides in the uncharged membranes, the first two principal components are influenced by almost all dihedral angles of the HVR domain. In contrast, in the charged membrane the first two principal components are dominated by backbone torsions from residues Pro207 to Asn210. Due to electrostatics the influence of the Arg209 Φ torsion is significant in the charged membrane compared to the other systems. When performing MD simulations of complex flexible structures an adequate sampling needs to be ensured. In order to verify that sampling was sufficient in the present study the Rab5 HVR$^{206-215}$ replicates in all membranes were subjected to one dPCA allowing for an actual sampling time of 4.5 µs (3x 6x 250 ns). The resulting free energy landscape is given in Supplementary Figure S15. Several energy minima were identified from which the five lowest energy wells were analyzed with regard to the corresponding structures. Each of these energy minima was populated with >500 conformations from more than one bilayer system. Furthermore, conformations from a specific bilayer could be found in different energy wells indicating that the simulation time was sufficient to sample multiple lowest energy conformations. Despite even shorter simulation times of 50 ns to 150 ns, early MD studies on membrane-anchored peptides [16, 19, 86] revealed insights into the flexibility of these structures and their interactions with a lipid environment. However, depending on the peptide amino acid composition and charge longer simulation times may be needed to elucidate the impact of the peptide insertion into the bilayer structure. Antimicrobial peptides are known to significantly perturb the bilayer structure partly accompanied by the formation of pores. Even microsecond-long MD simulations were not always sufficient to display a spontaneous peptide water-to-bilayer transfer or the complete re-organization of the surrounding membrane lipids after peptide insertion [87]. For the HVR$^{206-215}$ investigated here, however, an extensive disruption of the bilayer structure was not expected and not observed, since the inserted domain is not a charged peptide but a hydrocarbon anchor similar to the membrane lipids which makes longer simulation times not necessarily indispensable. But unquestionable, an extension of the simulation time may complete the

picture of membrane-bound Rab5 HVR dynamics and may also yield more membrane-specific interactions and conformations.

3.3.2 Diffusion of membrane-anchored HVR

To probe if membrane composition has an influence on the mobility of the $HVR^{206-215}$ we calculated the GG anchor lateral diffusion. Interestingly, the lateral diffusion is not only determined by the fraction of cholesterol, but also by the membrane charge. We see a clear slowing down of protein diffusion when the amount of cholesterol and also the charge of the membrane changes. With the cholesterol-induced increase in lipid order, the diffusion of the GG chains decreased by almost 50 % from $0.77 \cdot 10^{-7}$ cm^2s^{-1} (pure POPC) to $0.47 \cdot 10^{-7}$ cm^2s^{-1} (ternary mixture) and $0.43 \cdot 10^{-7}$ cm^2s^{-1} (charged membrane). With these diffusion rates, clearly a 200 ns MD simulation cannot ensure a thorough mixing of lipids around the protein. As a consequence, additional coarse-grained MD simulations which allow coverage of a longer timescale were performed to sufficiently sample lipid distribution and diffusion close to $HVR^{206-215}$.

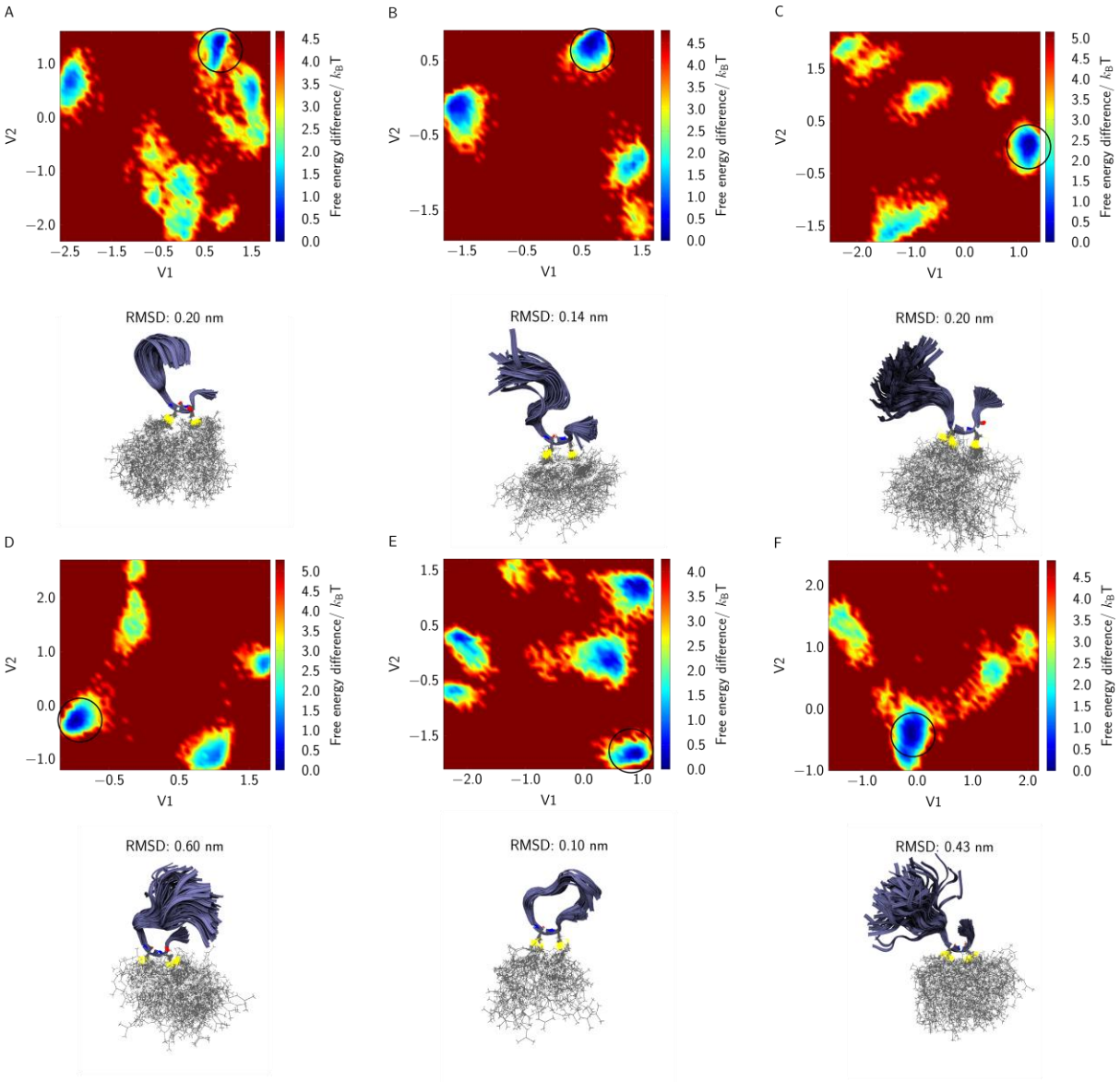

Figure 8 Dihedral PCA free energy landscapes of the six replicates Rab5 HVR$^{206\text{-}215}$ in the physiological membrane (**A-F**) The energy landscape is plotted as a function of the first two principal components (V1 and V2). The lowest energy structures of each HVR$^{206\text{-}215}$ replicate are shown below; the RMSD was measured for the structures belonging to one minimum energy conformation.

3.3.3 Local PI(3)P enrichment and phospholipid signaling

Biological membranes are characterized by a lateral non-uniform distribution of phospholipids of different types. In order to obtain a proper mixing of lipids and to allow the simulation of lipid species recruitment to the HVR$^{206\text{-}215}$, we performed 5 µs coarse-grained MD simulations. The lipid distribution as a function of the distance to the HVR$^{206\text{-}215}$ is shown in Figure 9A-C. For large distances the distribution approached that of the average membrane composition (compare to Table 1). However, close to the HVR domain within a radius of 1 nm an accumulation of cholesterol and PI(3)P was observed. At moderate distances the concentration of cholesterol decreased but increased again at larger

distances. This implies that cholesterol accumulation in the vicinity of $HVR^{206-215}$ resulted from recruitment from moderate distances to the peptide. The ratio of PI(3)P increased from an average of 5% to around 20% in close proximity to the protein; i.e. a 4-fold increase of PI(3)P within 1 nm of the $HVR^{206-215}$. Cholesterol and PI(3)P displaced the other lipids, thus their ratios were reduced close to the peptide. The PI(3)P distribution within the membrane averaged over the 5 µs coarse-grained simulation is shown in Figure 9D as a top view. It clearly shows that PI(3)P is significantly enriched in close proximity to the centered $HVR^{206-215}$. Here, it is noteworthy that there was no PI(3)P lipid within a distance cutoff of 1 nm, but 1 within 1.5 nm around the $HVR^{206-215}$ in the initial configuration (see Supplementary Table 7). In two additional replicate simulations with different initial lipid composition around the $HVR^{206-215}$ a similar PI(3)P enrichment was observed (see Supplementary Figure S16). Additionally, periods are found in which there was no PI(3)P lipid close the $HVR^{206-215}$. Thus, it is to exclude that the results purely come from overestimated MARTINI interactions or a biasing initial configuration. Interestingly, in contrast to PI(3)P, POPS was not enriched close to the peptide. Therefore, favorable electrostatic interactions seem to be formed exclusively between the phosphate group of the inositol ring and the positively charged arginine residue. Active lipid recruitment and clustering of proteins with specific lipids into microdomains have been observed in experimental and computational studies. The accumulation of negatively charged lipids has been observed for the nucleocapsid of the HIV-1 Gag polyprotein precursor [88]. In recent coarse-grained MD simulations the α-helical transmembrane domain of the cytokine receptor gp130 was also found to attract cholesterol and anionic lipids like PIP2 [89]. Similarly, the SNAP receptor protein syntaxin-1A co-localized with PIP2 to form microdomains, which facilitate membrane fusion [90]. In the case of the Rab5 $HVR^{206-215}$ the interactions between basic residues and PI(3)P stabilize membrane anchoring, slows down protein diffusion and may also create docking platforms for the Rab5-induced signaling in the early endosome.

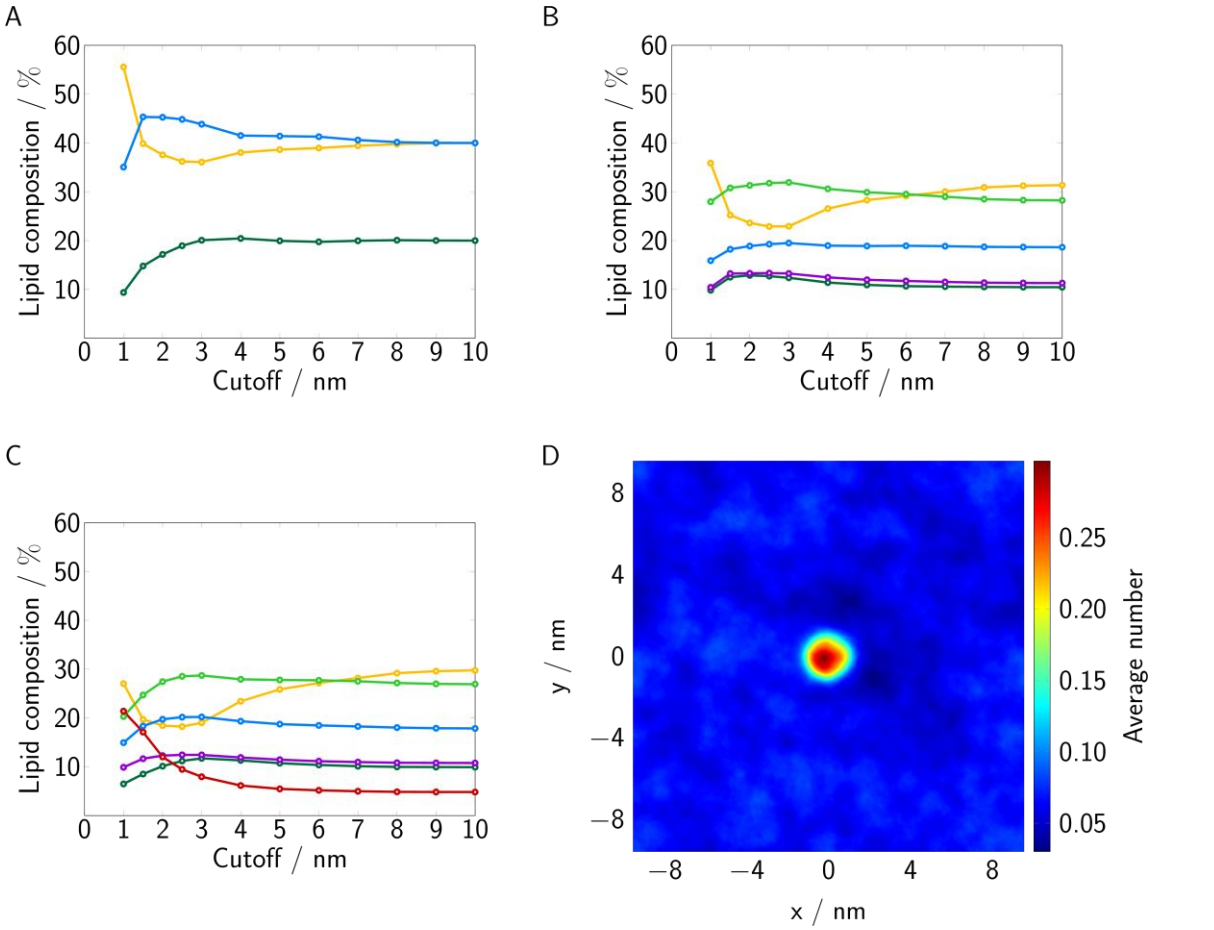

Figure 9 Membrane composition within a distance cutoff around the membrane-anchored HVR$^{206-215}$, averaged over 5 µs of CG simulation **(A-C)**. Data are shown for **A)** the ternary system, **B)** a five-component system without PI(3)P, and **C)** the charged six-component membrane. Lipid types are colored as follows: POPC (blue), cholesterol (yellow), PSM (dark green), POPE (light green), POPS (violet), and PI(3)P (red). **D)** Distribution of PI(3)P averaged over 5 µs of CG simulation in the charged six-component membrane as top view with the HVR being centered. A clear enrichment of PI(3)P around the HVR can be seen.

3.4. Free energy of HVR membrane binding

In order to estimate the Gibbs free energy of the peptide bilayer-to-water transition, ΔΔG, an umbrella sampling of HVR conformations at different distances from the membrane was performed. The extraction energy profiles of three arbitrarily chosen $HVR^{206-215}$ replicates in the three different model membranes were averaged (Figure 10). The membrane-inserted $HVR^{206-215}$ corresponded to the lowest energy structure for each membrane composition. The energy minimum was set to zero and all free energies were expressed as the difference to this minimum value. The energy gradually increased during the extraction process from the membrane and reached maximum values for the fully solvated peptide.

Experimental studies on the association of lipidated peptides with bilayers showed that each methylene carbon contributes 3.3 kJ/mol to the free energy change of saturated hydrocarbon chains [91]. Insertion of peptides modified with a GG prenyl chain into a POPC/POPE (9:1) bilayer gave free energy changes between -50 kJ/mol and -44 kJ/mol, depending on the C-terminus being either methylated or demethylated, respectively [68, 92]. Simulating the transfer from a pure POPC bilayer to water, i.e. the reverse process, in our simulations with the same tripeptide used by Silvius et al. [68] gave a free-energy change of 69 kJ/mol for a C-terminally methylated peptide and 61 kJ/mol for the demethylated peptide (data not shown). Thus, the simulations showed a slight overestimation of absolute free energy changes. The profile of the potential of mean force for the peptide bilayer-to-water transition is of type 3 referring to the shape-based scheme introduced by Neale et al. [93]. The energy minimum corresponds to a completely inserted, extended GG chain. A deeper insertion into the bilayer center results in an increase in energy. Extraction of the GG chains leads to increasingly water-exposed hydrocarbon groups with a high free energy barrier. The energy profiles obtained for our uncharged bilayer simulations reached a plateau between 116 kJ/mol and 119 kJ/mol for z distances larger than 1.6 nm-1.9 nm (see Figure 10). The energy profiles and relative free energies of anchor release did not significantly correlate with the bilayer thickness or the amount of cholesterol. In contrast, for $HVR^{206-215}$ in the charged membrane the free energy difference was larger and a plateau was reached at 124 kJ/mol for distances >2.8 nm. The reason for this behavior was a conformational extension of $HVR^{206-215}$ upon membrane extraction and a persistent interaction between the positively charged Arg209 and the negatively charged lipids POPS and PI(3)P in the physiological membrane (Figure 10B). Even when the GG chains were fully solvated both long range peptide-membrane electrostatic contacts, and two short-ranged stabilizing hydrogen bonds were formed between Arg209 and PI(3)P. Interactions between arginine and the phosphate groups of the zwitterionic lipids were not observed since these are buried within the bilayer, shielded by the lipid head groups and therefore not accessible for the HVR amino acids. The large PMF standard deviation in the charged membrane can be explained

by the local lipid composition (see Supplementary Table S6, anchors 1-3). For the first two HVR replicates (local PI(3)P concentration 12%, 5%), interactions between Arg209 and PI(3)P were more probable compared to the third one (local PI(3)P concentration 2%). This again stresses the dominance of the local lipid environment over the global membrane composition.

Our simulations are in agreement with studies of the GG-modified C-terminal region of the GTP-binding protein G25K. It was shown that binding was enhanced by several factors including i) an increased prenyl chain length, ii) methylation of the C-terminus, and iii) introduction of acidic lipids like POPS [94].

The convergence of the binding free energies of the peptide bilayer-to-water transfer needs to be discussed with regard to possible sampling errors. It has been shown for the bilayer insertion of different solutes that systematic sampling errors originating from an insufficient sampling may significantly influence ΔΔG [95]. Accordingly, the chosen equilibration time per umbrella window, the initial starting conformation and the bilayer size are of importance [93]. For small solutes inserted into a bilayer with only 32 lipids per leaflet an equilibration time of <125 ns per umbrella was shown to result in systematic sampling errors that shifted ΔΔG by several kcal/mol [95]. The reason for that long equilibration time is the conformational reorganization of the bilayer due to the extraction of the solute. In the present study membrane patches used for umbrella sampling were larger and contained up to approximately 100 lipids per leaflet. Consequently, longer equilibration times may yield more reliable ΔΔG values. Computational studies with long amphiphilic molecules have shown that for simulation times >70 ns the PMF profiles converged [96]. However, here, the focus was on the comparison of differently composed and charged membrane systems rather than on the calculation of absolute binding free energies. As we expect only systematic sampling errors due to the shorter equilibration time the different bilayer systems are influenced in a similar way.

It can be assumed that the GG chains cause small perturbations within the membrane and lipid reorganizations during the extraction process. The extent of such reorganizations should depend on the lipid composition and it may be speculated that the condensing effect of cholesterol could prevent larger structural rearrangements resulting in smaller energy barriers. However, such differences were not observed in the free-energy profiles of the present membrane systems. For amphiphiles being transferred from water to a POPC bilayer it was found that the amphiphile approaching the membrane attracts lipids [96]. This affects the membrane center of mass and, as this is included into the calculation of the reaction coordinate, influences the shape of the PMF. As a consequence, it was recommended to carefully select the reference plane for the reaction coordinate as it may be a possible source of errors [96].

Apart from umbrella sampling, an alternative method to estimate the PMF is to perform multiple non-equilibrium bidirectional pulling trajectories from SMD simulations and evaluate them by a combination of Minh-Adib's bidirectional estimator [97, 98] and WHAM equations. Instead of the number of windows and the equilibration time in umbrella sampling, the number of pulling trajectories and the pulling velocity are crucial for the convergence and reliability of the resulting free-energy profiles. In this context it has been shown that results from a few slower pulling trajectories (v=10 Å/ns) are superior to many relatively fast pulling velocity trajectories (v=100 Å/ns) in obtaining accurate PMFs [98]. However, this alternative seems to provide good estimates when the transition path, i.e. in the present case the bilayer-to-water transfer, is not affected by hysteresis. Hysteresis in the PMF using umbrella sampling was observed for amphiphiles interacting with membranes. Here, shifting the molecule from the bilayer to water yielded results comparable to experimental data, whereas the opposite transfer from water to the membrane environment suffered from sampling problems close to the membrane-water interface. These effects may also play a role in the free-energy profile of the GG chain bilayer extraction and should be subjected to further investigations.

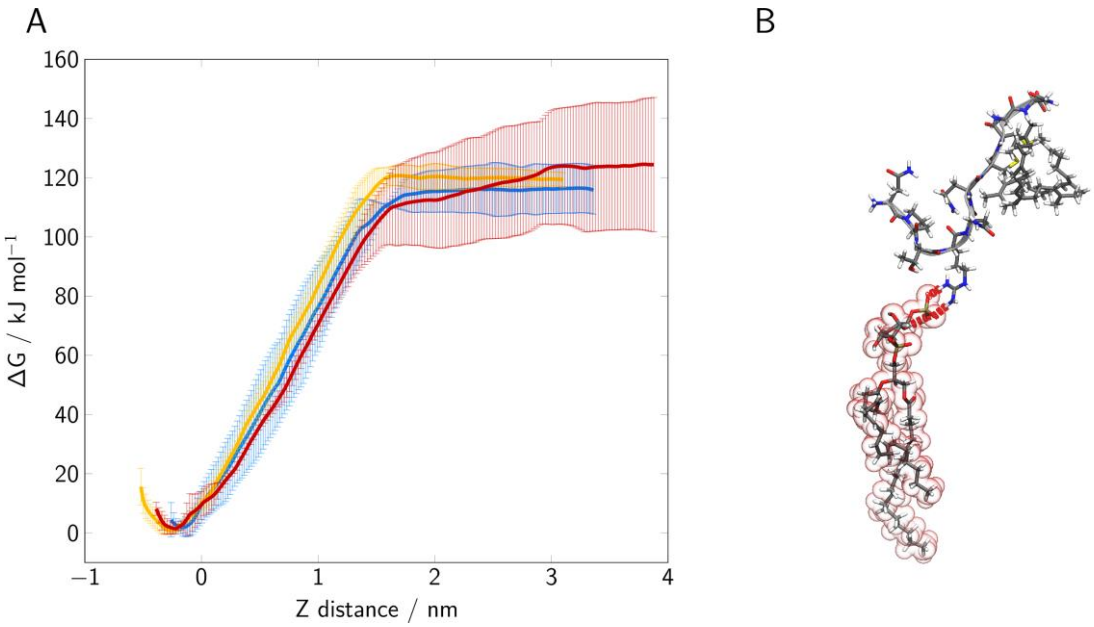

Figure 10 Estimated free energy difference upon extraction of GG HVR from pure POPC (blue), the ternary mixture (yellow) and the charged membrane (red). The minimum energy with fully inserted GG chains was set to zero and all other energies are expressed as differences to this minimum **(A)**. In the charged membrane electrostatic interactions are formed between Arg209 of the peptide and the inositol ring phosphate of PI(3)P **(B)**.

Conclusion

Rab small GTPases are the key regulators of endosomal sorting and trafficking. The dysfunction or aberrant control of Rab cycling leads to the appearance of several non-physiological states ranging from infectious diseases to cancer [99]. The C-terminal HVR of Rab proteins is post-translationally modified and proposed to function as a signal for targeting Rab proteins to specific subcellular membranes [1]. Replacement of the C-terminal 35 residues of early endosomal (EE) Rab5 with that of Rab7 resulted in re-localization of the hybrid Rab to the late endosome (LE). However, specific plasma membrane targeting is not only mediated by a cysteine-cysteine motif but additional specific interactions of amino acid residues in the vicinity of the GG site. A deletion of ten residues ($\Delta HVR^{201-211}$) of Rab5 obstructed membrane anchoring and left Rab5 in the cytosol despite the retention of the post-translational modification.

Full-atomistic and coarse-grained MD simulations provide a comprehensive picture of structural and dynamical properties of the GG-Rab5 C-terminal $HVR^{206-215}$ in membranes of different lipid compositions. Membrane association causes only minor local structural rearrangements of surrounding phospholipids within a radius of 3 nm. The overall membrane structure remains unchanged which was also observed for lipidated C-terminal N-Ras [15-17]. The HVR is the flexible linker connecting the catalytically active protein G domain and the membrane GG anchor which leads to a multitude of G domain orientations with respect to the membrane surface [11-14]. In our simulations Rab5 $HVR^{206-215}$ adopted an intrinsically disordered structure lacking any secondary structure elements in each of the different membrane compositions. Diffusion of the HVR is influenced both by the amount of cholesterol, i.e. the resulting increase in lipid order, and the presence of negatively charged lipids (PI(3)P). The positively charged Rab5 residue Arg209 was shown to interact with the solvent-exposed phosphate group of the PI(3)P inositol ring which prevented Arg209 membrane insertion but increased the HVR free energy of binding.

The family of Rab proteins in human has about 62 members, some of which are characteristic for the early or the late endosome. Rab5, 21 and 22 are EE-specific and display almost identical interaction properties. In particular, around the switch regions they show highly conserved electrostatic potentials and only subtle differences around switch I and the interswitch regions. LE Rab proteins (like Rab7), however, show strikingly different electrostatic potentials and thus probably do not share any regulators with EE Rab GTPases [100].

This difference in interaction fields may also be an adjustment to the membrane composition difference between early and late endosomes. The EE has a PI(3)P content of about 5% and the interaction energy between $HVR^{206-215}$ and the negatively charged membrane was

calculated to be about 124 kJ/mol. This amount would have to be overcome by GDI upon Rab5 extraction from the membrane into the cytosol. LEs, on the other side, are enriched in negatively charged PI(3,5)P. The terminal 18 residues of the HVR of Rab7 (**K**LD**K**ND**R**A**K**ASAESCSC; prenylated cysteines underlined, positive amino acids bold) display an accumulation of amino acids with positively charged side chains. For Rab5 (VDLTEPTQPT**R**NQCCSN), strong electrostatic interaction with 5% PI(3)P in the EE is only feasible via Arg209 while Rab7 may form such interactions via lysine residues 191, 194 and 199 and arginine 197. GDI extraction of membrane-recruited EE Rab5 may thus be feasible while Rab7 would remain membrane-associated and increase in concentration upon endosome maturation.

There is increasing evidence that membrane-bound molecules are not randomly distributed in the membrane bilayer but are enriched in membrane domains of varying lipid composition [101]. Whereas standard lipid raft formation originates from intercalation of sphingolipids with cholesterol and leads to a separation of phases, Rab5 regulates membrane arrangement by a different mechanism. According to our findings, protein-lipid interactions are a central factor for the accumulation of Rab5 in PI(3)P microdomains. They are small in size (~10 nm) and dynamic in nature.

We propose that Rab5 and its effectors are not randomly recruited and distributed on the early endosome membrane but are spatially segregated in a defined membrane domain. Membrane domains are beginning to be recognized as platforms for spatial control of cellular signaling processes.

Acknowledgements

We thank The Max Planck Society for the Advancement of Science, the Excellence Initiative “Research Center for Dynamic Systems: Systems Engineering” by the state of Saxony-Anhalt and the “European Regional Development Fund (ERDF)” for financial support. ES is supported by the International Max Planck Research School (IMPRS) for Advanced Methods in Process and Systems Engineering, Magdeburg, Germany. We thank the MPDCF for providing computing resources.

References

1. Chavrier, P., et al., *Hypervariable C-terminal domain of rab proteins acts as a targeting signal.* Nature, 1991. **353**(6346): p. 769-772.
2. Ali, B.R., et al., *Multiple regions contribute to membrane targeting of Rab GTPases.* Journal of Cell Science, 2004. **117**(26): p. 6401-6412.
3. Li, F., et al., *The role of the hypervariable C-terminal domain in Rab GTPases membrane targeting.* Proceedings of the National Academy of Sciences of the United States of America, 2014. **111**(7): p. 2572-2577.
4. Simons, K. and G. Van Meer, *Lipid Sorting in Epithelial Cells.* Biochemistry, 1988. **27**(17): p. 6197-6202.
5. Simons, K. and E. Ikonen, *Functional rafts in cell membranes.* Nature, 1997. **387**(6633): p. 569-572.
6. Levental, I., M. Grzybek, and K. Simons, *Greasing Their Way: Lipid Modifications Determine Protein Association with Membrane Rafts.* Biochemistry, 2010. **49**(30): p. 6305-6316.
7. Triffo, S.B., et al., *Monitoring Lipid Anchor Organization in Cell Membranes by PIE-FCCS.* Journal of the American Chemical Society, 2012. **134**(26): p. 10833-10842.
8. Baumgart, T., et al., *Large-scale fluid/fluid phase separation of proteins and lipids in giant plasma membrane vesicles.* Proceedings of the National Academy of Sciences of the United States of America, 2007. **104**(9): p. 3165-3170.
9. Johnson, S.A., et al., *Temperature-dependent phase behavior and protein partioning in giant plasma membrane vesicles.* Biochimica Et Biophysica Acta-Biomembranes, 2010. **1798**(7): p. 1427-1435.
10. Stenmark, H., *Rab GTPases as coordinators of vesicle traffic.* Nature Reviews Molecular Cell Biology, 2009. **10**(8): p. 513-525.
11. Edler, E. and M. Stein, *Probing the druggability of membrane-bound Rab5 by molecular dynamics simulations.* Journal of Enzyme Inhibition and Medicinal Chemistry, 2017. **32**(1): p. 434-443.
12. Gorfe, A.A., et al., *Structure and dynamics of the full-length lipid-modified H-ras protein in a 1,2-dimyristoylglycero-3-phosphocholine bilayer.* Journal of Medicinal Chemistry, 2007. **50**(4): p. 674-684.
13. Prakash, P., et al., *Oncogenic K-Ras Binds to an Anionic Membrane in Two Distinct Orientations: A Molecular Dynamics Analysis.* Biophysical Journal, 2016. **110**(5): p. 1125-1138.
14. Prakash, P. and A.A. Gorfe, *Membrane orientation dynamics of lipid-modified small GTPases.* Small GTPases, 2016: p. 1-10.
15. Huster, D., et al., *Membrane insertion of a lipidated ras peptide studied by FTIR, solid-state NMR, and neutron diffraction spectroscopy.* Journal of the American Chemical Society, 2003. **125**(14): p. 4070-4079.
16. Gorfe, A.A., R. Pellarin, and A. Caflisch, *Membrane localization and flexibility of a lipidated ras peptide studied by molecular dynamics simulations.* Journal of the American Chemical Society, 2004. **126**(46): p. 15277-15286.
17. Reuther, G., et al., *Structural model of the membrane-bound C terminus of lipid-modified human N-ras protein.* Angewandte Chemie-International Edition, 2006. **45**(32): p. 5387-5390.
18. Reuther, G., et al., *The lipidated membrane anchor of full length N-Ras protein shows an extensive dynamics as revealed by solid-state NMR spectroscopy.* Journal of the American Chemical Society, 2006. **128**(42): p. 13840-13846.
19. Vogel, A., et al., *Flexibility of ras lipid modifications studied by H-2 solid-state NMR and molecular dynamics simulations.* Biophysical Journal, 2007. **93**(8): p. 2697-2712.

20. Janosi, L. and A.A. Gorfe, *Segregation of Negatively Charged Phospholipids by the Polycationic and Farnesylated Membrane Anchor of Kras.* Biophysical Journal, 2010. **99**(11): p. 3666-3674.
21. Pöyry, S. and I. Vattulainen, *Role of charged lipids in membrane structures — Insight given by simulations.* Biochimica et Biophysica Acta (BBA) - Biomembranes.
22. Best, R.B., et al., *Optimization of the Additive CHARMM All-Atom Protein Force Field Targeting Improved Sampling of the Backbone phi, psi and Side-Chain chi(1) and chi(2) Dihedral Angles.* Journal of Chemical Theory and Computation, 2012. **8**(9): p. 3257-3273.
23. Pastor, R.W. and A.D. MacKerell, *Development of the CHARMM Force Field for Lipids.* Journal of Physical Chemistry Letters, 2011. **2**(13): p. 1526-1532.
24. *TURBOMOLE V6.6 2014, a development of University of Karlsruhe and Forschungszentrum Karlsruhe GmbH, 1989-2007, TURBOMOLE GmbH, since 2007; available from http://www.turbomole.com.*
25. Weigend, F. and R. Ahlrichs, *Balanced basis sets of split valence, triple zeta valence and quadruple zeta valence quality for H to Rn: Design and assessment of accuracy.* Physical Chemistry Chemical Physics, 2005. **7**(18): p. 3297-3305.
26. Becke, A.D., *Density-functional exchange-energy approximation with correct asymptotic behavior.* Physical Review A, 1988. **38**(6): p. 3098-3100.
27. Perdew, J.P., *Density-functional approximation for the correlation energy of the inhomogeneous electron gas.* Physical Review B, 1986. **33**(12): p. 8822-8824.
28. Schafer, A., et al., *COSMO Implementation in TURBOMOLE: Extension of an efficient quantum chemical code towards liquid systems.* Physical Chemistry Chemical Physics, 2000. **2**(10): p. 2187-2193.
29. Tanizaki, S. and M. Feig, *A generalized Born formalism for heterogeneous dielectric environments: Application to the implicit modeling of biological membranes.* Journal of Chemical Physics, 2005. **122**(12): p. 13.
30. Humphrey, W., A. Dalke, and K. Schulten, *VMD: Visual molecular dynamics.* Journal of Molecular Graphics & Modelling, 1996. **14**(1): p. 33-38.
31. Jo, S., et al., *CHARMM-GUI Membrane Builder for Mixed Bilayers and Its Application to Yeast Membranes.* Biophysical Journal, 2009. **97**(1): p. 50-58.
32. Wu, E.L., et al., *CHARMM-GUI Membrane Builder Toward Realistic Biological Membrane Simulations.* Journal of Computational Chemistry, 2014. **35**(27): p. 1997-2004.
33. Chiantia, S. and E. London, *Sphingolipids and membrane domains: recent advances.* Handbook of experimental pharmacology, 2013(215): p. 33-55.
34. Ingolfsson, H.I., et al., *Lipid Organization of the Plasma Membrane.* Journal of the American Chemical Society, 2014. **136**(41): p. 14554-14559.
35. Phillips, J.C., et al., *Scalable molecular dynamics with NAMD.* Journal of Computational Chemistry, 2005. **26**(16): p. 1781-1802.
36. Venable, R.M., et al., *CHARMM All-Atom Additive Force Field for Sphingomyelin: Elucidation of Hydrogen Bonding and of Positive Curvature.* Biophysical Journal, 2014. **107**(1): p. 134-145.
37. Lim, J.B., B. Rogaski, and J.B. Klauda, *Update of the Cholesterol Force Field Parameters in CHARMM.* Journal of Physical Chemistry B, 2012. **116**(1): p. 203-210.
38. Jorgensen, W.L., et al., *Comparison of simple potential functions for simulating liquid water.* Journal of Chemical Physics, 1983. **79**(2): p. 926-935.
39. Martyna, G.J., D.J. Tobias, and M.L. Klein, *Constant pressure molecular dynamics algorithms.* Journal of Chemical Physics, 1994. **101**(5): p. 4177-4189.
40. Feller, S.E., et al., *Constant pressure molecular dynamics simulation: The Langevin piston method.* Journal of Chemical Physics, 1995. **103**(11): p. 4613-4621.
41. Darden, T., D. York, and L. Pedersen, *Particle mesh Ewald: An N.log(N) method for Ewald sums in large systems.* Journal of Chemical Physics, 1993. **98**(12): p. 10089-10092.

42. Essmann, U., et al., *A smooth particle mesh Ewald method.* Journal of Chemical Physics, 1995. **103**(19): p. 8577-8593.
43. Park, S., et al., *Free energy calculation from steered molecular dynamics simulations using Jarzynski's equality.* Journal of Chemical Physics, 2003. **119**(6): p. 3559-3566.
44. Grubmuller, H., B. Heymann, and P. Tavan, *Ligand binding: Molecular mechanics calculation of the streptavidin biotin rupture force.* Science, 1996. **271**(5251): p. 997-999.
45. Marrink, S.J., et al., *Adhesion forces of lipids in a phospholipid membrane studied by molecular dynamics simulations.* Biophysical Journal, 1998. **74**(2): p. 931-943.
46. Lorenzo, A.C. and P.M. Bisch, *Analyzing different parameters of steered molecular dynamics for small membrane interacting molecules.* Journal of Molecular Graphics & Modelling, 2005. **24**(1): p. 59-71.
47. Kumar, S., et al., *The weighted histogram analysis method for free-energy calculations on biomolecules. I. The method.* Journal of Computational Chemistry, 1992. **13**(8): p. 1011-1021.
48. *Grossfield, A. "WHAM: an implementation of the weighted histogram analysis method", http://membrane.urmc.rochester.edu/content/wham/, version 2.0.9*.
49. Wassenaar, T.A., et al., *Computational Lipidomics with insane: A Versatile Tool for Generating Custom Membranes for Molecular Simulations.* Journal of Chemical Theory and Computation, 2015. **11**(5): p. 2144-2155.
50. Marrink, S.J., et al., *The MARTINI Force Field: Coarse Grained Model for Biomolecular Simulations.* The Journal of Physical Chemistry B, 2007. **111**(27): p. 7812-7824.
51. de Jong, D.H., et al., *Improved Parameters for the Martini Coarse-Grained Protein Force Field.* Journal of Chemical Theory and Computation, 2013. **9**(1): p. 687-697.
52. Van der Spoel, D., et al., *GROMACS: Fast, flexible, and free.* Journal of Computational Chemistry, 2005. **26**(16): p. 1701-1718.
53. de Jong, D.H., et al., *Martini straight: Boosting performance using a shorter cutoff and GPUs.* Computer Physics Communications, 2016. **199**: p. 1-7.
54. Berendsen, H.J.C., et al., *Molecular dynamics with coupling to an external bath.* Journal of Chemical Physics, 1984. **81**(8): p. 3684-3690.
55. Parrinello, M. and A. Rahman, *Polymorphic transitions in single crystals: a new molecular dynamics method.* Journal of Applied Physics, 1981. **52**(12): p. 7182-7190.
56. Michaud-Agrawal, N., et al., *Software News and Updates MDAnalysis: A Toolkit for the Analysis of Molecular Dynamics Simulations.* Journal of Computational Chemistry, 2011. **32**(10): p. 2319-2327.
57. Allen, W.J., J.A. Lemkul, and D.R. Bevan, *GridMAT-MD: A Grid-Based Membrane Analysis Tool for Use With Molecular Dynamics.* Journal of Computational Chemistry, 2009. **30**(12): p. 1952-1958.
58. Douliez, J.P., A. Ferrarini, and E.J. Dufourc, *On the relationship between C-C and C-D order parameters and its use for studying the conformation of lipid acyl chains in biomembranes.* Journal of Chemical Physics, 1998. **109**(6): p. 2513-2518.
59. Miller, S., et al., *Interior and Surface of Monomeric Proteins.* Journal of Molecular Biology, 1987. **196**(3): p. 641-656.
60. Mu, Y.G., P.H. Nguyen, and G. Stock, *Energy landscape of a small peptide revealed by dihedral angle principal component analysis.* Proteins-Structure Function and Bioinformatics, 2005. **58**(1): p. 45-52.
61. Altis, A., et al., *Dihedral angle principal component analysis of molecular dynamics simulations.* Journal of Chemical Physics, 2007. **126**(24): p. 10.
62. Sittel, F., A. Jain, and G. Stock, *Principal component analysis of molecular dynamics: On the use of Cartesian vs. internal coordinates.* Journal of Chemical Physics, 2014. **141**(1): p. 9.
63. Saxton, M.J., *Single-particle tracking: The distribution of diffusion coefficients.* Biophysical Journal, 1997. **72**(4): p. 1744-1753.

64. Siebrasse, J.P., et al., *Discontinuous movement of mRNP particles in nucleoplasmic regions devoid of chromatin.* Proceedings of the National Academy of Sciences of the United States of America, 2008. **105**(51): p. 20291-20296.
65. Monticelli, L., et al., *The MARTINI coarse-grained force field: Extension to proteins.* Journal of Chemical Theory and Computation, 2008. **4**(5): p. 819-834.
66. Kabsch, W. and C. Sander, *Dictionary of protein secondary structure: Pattern recognition of hydrogen-bonded and geometrical features.* Biopolymers, 1983. **22**(12): p. 2577-2637.
67. Hub, J.S., B.L. de Groot, and D. van der Spoel, *g_wham-A Free Weighted Histogram Analysis Implementation Including Robust Error and Autocorrelation Estimates.* Journal of Chemical Theory and Computation, 2010. **6**(12): p. 3713-3720.
68. Silvius, J.R. and F. Lheureux, *Fluorometric Evaluation of the Affinities of Isoprenylated Peptides for Lipid Bilayers.* Biochemistry, 1994. **33**(10): p. 3014-3022.
69. Kucerka, N., M.P. Nieh, and J. Katsaras, *Fluid phase lipid areas and bilayer thicknesses of commonly used phosphatidylcholines as a function of temperature.* Biochimica Et Biophysica Acta-Biomembranes, 2011. **1808**(11): p. 2761-2771.
70. McIntosh, T.J., *The effect of cholesterol on the structure of phosphatidylcholine bilayers.* Biochimica Et Biophysica Acta, 1978. **513**(1): p. 43-58.
71. Hung, W.C., et al., *The condensing effect of cholesterol in lipid bilayers.* Biophysical Journal, 2007. **92**(11): p. 3960-3967.
72. Krause, M.R. and S.L. Regen, *The Structural Role of Cholesterol in Cell Membranes: From Condensed Bilayers to Lipid Rafts.* Accounts of Chemical Research, 2014. **47**(12): p. 3512-3521.
73. Ferreira, T.M., et al., *Cholesterol and POPC segmental order parameters in lipid membranes: solid state H-1-C-13 NMR and MD simulation studies.* Physical Chemistry Chemical Physics, 2013. **15**(6): p. 1976-1989.
74. Aittoniemi, J., et al., *Insight into the putative specific interactions between cholesterol, sphingomyelin, and palmitoyl-oleoyl phosphatidylcholine.* Biophysical Journal, 2007. **92**(4): p. 1125-1137.
75. Wu, E.L., et al., *Preferred Orientations of Phosphoinositides in Bilayers and Their Implications in Protein Recognition Mechanisms.* Journal of Physical Chemistry B, 2014. **118**(16): p. 4315-4325.
76. van der Spoel, D., P.J. van Maaren, and H.J.C. Berendsen, *A systematic study of water models for molecular simulation: Derivation of water models optimized for use with a reaction field.* Journal of Chemical Physics, 1998. **108**(24): p. 10220-10230.
77. Holz, M., S.R. Heil, and A. Sacco, *Temperature-dependent self-diffusion coefficients of water and six selected molecular liquids for calibration in accurate H-1 NMR PFG measurements.* Physical Chemistry Chemical Physics, 2000. **2**(20): p. 4740-4742.
78. Filippov, A., G. Oradd, and G. Lindblom, *The effect of cholesterol on the lateral diffusion of phospholipids in oriented bilayers.* Biophysical Journal, 2003. **84**(5): p. 3079-3086.
79. Vogel, A., et al., *Lipid modifications of a Ras peptide exhibit altered packing and mobility versus host membrane as detected by 2H solid-state NMR.* Journal of the American Chemical Society, 2005. **127**(35): p. 12263-12272.
80. Vogel, A., et al., *The Lipid Modifications of Ras that Sense Membrane Environments and Induce Local Enrichment.* Angewandte Chemie-International Edition, 2009. **48**(46): p. 8784-8787.
81. Ramachandran, G.N., C. Ramakrishnan, and V. Sasisekharan, *Stereochemistry of polypeptide chain configurations.* Journal of Molecular Biology, 1963. **7**(1): p. 95-&.
82. Lumb, C.N. and M.S.P. Sansom, *Finding a Needle in a Haystack: The Role of Electrostatics in Target Lipid Recognition by PH Domains.* Plos Computational Biology, 2012. **8**(7): p. 10.
83. Yang, P., et al., *Effect of Lipid Composition on the Membrane Orientation of the G Protein-Coupled Receptor Kinase 2-G beta(1)gamma(2) Complex.* Biochemistry, 2016. **55**(20): p. 2841-2848.

84. Kalli, A.C., G. Morgan, and M.S.P. Sansom, *Interactions of the Auxilin-1 PTEN-like Domain with Model Membranes Result in Nanoclustering of Phosphatidyl Inositol Phosphates.* Biophysical Journal, 2013. **105**(1): p. 137-145.
85. Murray, D., et al., *Electrostatic interaction of myristoylated proteins with membranes: simple physics, complicated biology.* Structure, 1997. **5**(8): p. 985-989.
86. Jensen, M.O., O.G. Mouritsen, and G.H. Peters, *Simulations of a membrane-anchored peptide: Structure, dynamics, and influence on bilayer properties.* Biophysical Journal, 2004. **86**(6): p. 3556-3575.
87. Bennett, W.F.D., et al., *Antimicrobial Peptide Simulations and the Influence of Force Field on the Free Energy for Pore Formation in Lipid Bilayers.* Journal of Chemical Theory and Computation, 2016. **12**(9): p. 4524-4533.
88. Kempf, N., et al., *The HIV-1 Nucleocapsid Protein Recruits Negatively Charged Lipids To Ensure Its Optimal Binding to Lipid Membranes.* Journal of Virology, 2015. **89**(3): p. 1756-1767.
89. Koldso, H., et al., *Lipid Clustering Correlates with Membrane Curvature as Revealed by Molecular Simulations of Complex Lipid Bilayers.* Plos Computational Biology, 2014. **10**(10): p. 11.
90. van den Bogaart, G., et al., *Membrane protein sequestering by ionic protein-lipid interactions.* Nature, 2011. **479**(7374): p. 552-555.
91. Peitzsch, R.M. and S. McLaughlin, *Binding of Acylated Peptides and Fatty Acids to Phospholipid Vesicles: Pertinence to Myristoylated Proteins.* Biochemistry, 1993. **32**(39): p. 10436-10443.
92. Shahinian, S. and J.R. Silvius, *Doubly-Lipid-Modified Protein Sequence Motifs Exhibit Long-Lived Anchorage to Lipid Bilayer Membranes.* Biochemistry, 1995. **34**(11): p. 3813-3822.
93. Neale, C. and R. Pomes, *Sampling errors in free energy simulations of small molecules in lipid bilayers.* Biochimica Et Biophysica Acta-Biomembranes, 2016. **1858**(10): p. 2539-2548.
94. Ghomashchi, F., et al., *Binding of Prenylated and Polybasic Peptides to Membranes: Affinities and Intervesicle Exchange.* Biochemistry, 1995. **34**(37): p. 11910-11918.
95. Neale, C., et al., *Statistical Convergence of Equilibrium Properties in Simulations of Molecular Solutes Embedded in Lipid Bilayers.* Journal of Chemical Theory and Computation, 2011. **7**(12): p. 4175-4188.
96. Filipe, H.A.L., et al., *How To Tackle the Issues in Free Energy Simulations of Long Amphiphiles Interacting with Lipid Membranes: Convergence and Local Membrane Deformations.* Journal of Physical Chemistry B, 2014. **118**(13): p. 3572-3581.
97. Minh, D.D.L. and A.B. Adib, *Optimized free energies from bidirectional single-molecule force spectroscopy.* Physical Review Letters, 2008. **100**(18): p. 4.
98. Ngo, V.A., et al., *Estimation of Potentials of Mean Force from Nonequilibrium Pulling Simulations Using Both Minh-Adib Estimator and Weighted Histogram Analysis Method.* Journal of Chemical Theory and Computation, 2016. **12**(3): p. 1000-1010.
99. Hutagalung, A.H. and P.J. Novick, *Role of Rab GTPases in Membrane Traffic and Cell Physiology.* Physiological Reviews, 2011. **91**(1): p. 119-149.
100. Stein, M., et al., *The Interaction Properties of the Human Rab GTPase Family - A Comparative Analysis Reveals Determinants of Molecular Binding Selectivity.* Plos One, 2012. **7**(4): p. 13.
101. Mukherjee, S. and F.R. Maxfield, *Role of membrane organization and membrane domains in endocytic lipid trafficking.* Traffic, 2000. **1**(3): p. 203-211.